Supplemental Information for "Realizing Low-Energy Drip Irrigation via a 1-Dimensional Model of Low-Pressure Drip Emitters"

Aditya Ghodgaonkar[1*], Julia Sokol[1,2], Susan Amrose[1], Amos G. Winter V[1*]

[1*]Department of Mechanical Engineering, Massachusetts Institute of Technology, 77 Massachusetts Avenue, Cambridge, 02139, Massachusetts, U.S.A..
[2]Form Energy, Somerville, 02143, Massachusetts, U.S.A..

*Corresponding author(s). E-mail(s): adighod@mit.edu; awinter@mit.edu;
Contributing authors: juliasokol@gmail.com; samrose@mit.edu;

1 Numerical Algorithm for Fluid-Structure Interaction and Performance Evaluation

The flow rate at every pressure is one of the roots of the equation

$$f(Q) : K_{tot}Q^2 - P_{in} = 0. \tag{1}$$

The total resistance K_{tot} depends on the diaphragm deflection $w(r)$ and the flow rate Q itself. The fluid-structure interaction (FSI) algorithm partitions the interdependency between flow resistances and diaphragm deflection so that each may be calculated independently using 1D analytical expressions. This kind of partitioned approach is favored over a monolithic approach (where all equations are simultaneously solved using a matrix-inversion step) due to ease of implementation [1].

Figure 1 presents the FSI algorithm implemented in this model.

1. The i^{th} pressure step P_i is initiated with the emitter design parameters and a starting guess for the flow rate $Q_{i,j=0}$. The subscript j refers to the iteration number.

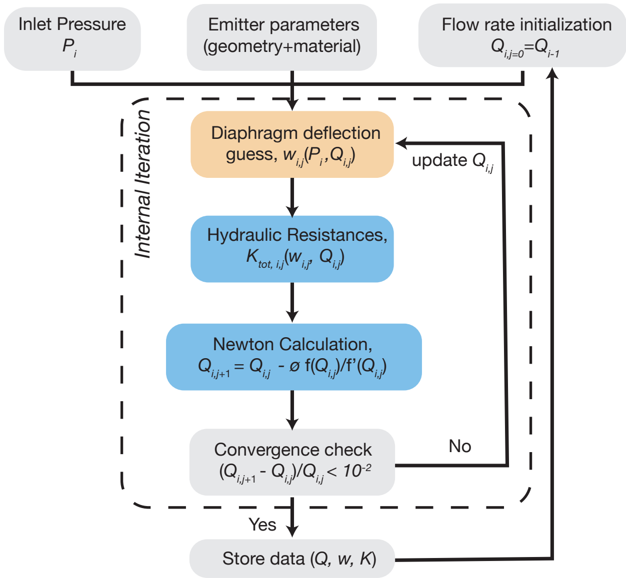

Fig. 1 Partioned FSI algorithm for modeling PC emitters.

2. At iteration j, the model uses $Q_{i,j-1}$ to calculate the diaphragm load $q_{load,j} = K_{lab}Q^2_{i,j-1}$ and thereby the diaphragm deflection $w_{i,j}(r)$.
3. Individual hydraulic resistances are calculated using $w_{i,j}(r)$ and $Q_{i,j-1}$ and summed up to obtain the total resistance $K_{tot,i,j}$.
4. Newton calculation with Successive Over-Relaxation (SOR, ϕ) is performed to obtain the updated flow rate

$$Q_{i,j} = Q_{i,j-1} - \phi \frac{f(Q_{i,j-1})}{f'(Q_{i,j-1})}, \text{ where} \tag{2}$$

$$f(Q_{i,j-1}) = K_{tot,i,j}Q^2_{i,j-1} - P_i, \tag{3}$$

$$f'(Q_{i,j-1}) = 2K_{tot,i,j}Q_{i,j-1}. \tag{4}$$

5. This process is repeated till:

$$\left| \frac{Q_{i,j} - Q_{i,j-1}}{Q_{i,j-1}} \right| \leq 0.01. \tag{5}$$

6. At the end of the pressure step, the new flow rate is used to initialize the next pressure step.

Newton's method is used to solve Eq. 1 because this method converges quadratically, resulting in faster calculations. This is possible because Eq. 1 has a non-zero slope ($f' = 2K_{tot}Q > 0$) and a continuous curvature ($f'' = 2K_{tot}$). SOR is implemented because Eq. 1 is nonlinear. The hydraulic resistance K_{tot} features the diaphragm cavity resistance K_{dia} or weir resistance K_{weir}, both of which depend on the flow rate.

Implementing SOR reduces the change in flow rate between iterations and encourages stability, albeit at the cost of some more execution time. The SOR factor $\phi = 0.1$ was selected through tuning runs.

Performance evaluation: The model provides a series of flow rate values $\{Q_i\}$ at each pressure value $\{P_i\}$. To calculate the activation pressure $P_{act,model}$, a pre-activation curve $Q_{pre} = \mathcal{C}P_{in}^{1/2}$ is fit to the first few calculated flow rates ($\mathcal{C}$ is a constant of proportionality). The predicted activation pressure $P_{act,model}$ is the pressure at which the difference between the predicted flow rate Q_i and pre-activation curve fitted flow rate Q_{pre} exceeds a chosen threshold:

$$P_{act,model} = P_i \text{ when } |Q_i - \mathcal{C}P_i^{1/2}| > 0.1 \text{ L/hr.} \tag{6}$$

The rated flow rate $Q_{rated,model}$ is the mean flow rate above the predicted activation pressure:

$$Q_{rated,model} = \sum_{P_i \geq P_{act,model}} \frac{Q_i}{N}. \tag{7}$$

The predicted exponent n_{model} is obtained by fitting a power-law curve to the post-activation pressure-flow rate. To avoid over-fitting, pressure values selected for curve fit are coarsely sampled from $\{P_i\}$ (spaced 0.25 bar apart).

2 Characterization of Diaphragm Material

Diaphragms used in this paper were sourced from Toro Blueline PC emitters [2] and were 1 mm thick. In characterization experiments, the diaphragm was placed on a 3D-printed holder and probed on a texture analyzer instrument. The texture analyzer had a 50 N load cell (Fig. 2A). Clearance around the diaphragm on the holder was kept the same as the diaphragm clearance in the emitter prototypes to maintain identical boundary conditions. A probe with a 0.7 mm diameter ball-end (Fig. 2B,C) was centered above the diaphragm and deflected the diaphragm till its center deflection $w_0 = 1$ mm. The deflection rate was 0.2 mm/sec. The load required to do this (F_{load}, N) was measured. The maximum vertical deflection was set to 1 mm to match the largest expected lands depth that might be designed into the emitter prototypes. Four replicate measurements were made (Fig. 2D).

The diaphragm's bending stiffness D_{dia} (N-m) was derived by fitting a linear slope to the average $F_{load} - w_0$ data (Fig. 2E). To do this, the case of a simply supported circular plate with a concentrated central load [3](Pg. 491, Case 16) was invoked:

$$D_{dia} = -\underbrace{\frac{F_{load}}{w_0}}_{\text{measured}} \frac{r_{dia}^2}{16} \frac{3+\nu}{1+\nu}, \tag{8}$$

where w_0 was the imposed central deflection (m), F_{load} was the measured load (N), $r_{dia} = 3.85 \times 10^{-3}$ m was the radius of the circular diaphragm edge support, and $\nu = 0.49$ was the Poisson ratio (from supplier data [4]). The elastic modulus was then

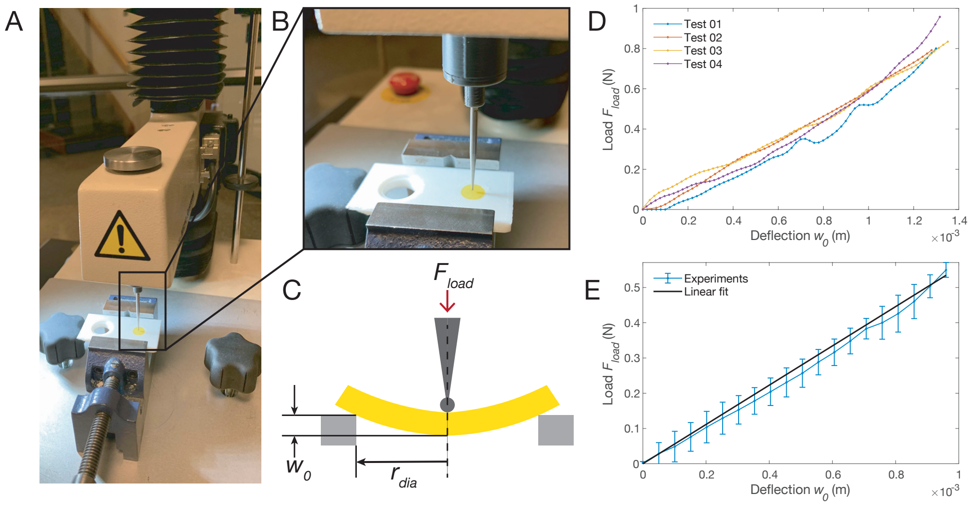

Fig. 2 Characterization of diaphragm material. A) The silicone rubber diaphragm was tested on a texture analyzer by measuring the load required to deflect it through 1 mm at its center (B close up). C) Test schematic with prescribed deflection (w_0) and measured load (F_{load}). D) Raw data was averaged, and (E) a linear fit was made to obtain the effective linear stiffness.

derived using the definition of D_{dia}

$$E_{dia} = \frac{12 D_{dia}(1-\nu^2)}{t_{dia}^3}, \tag{9}$$

where $t_{dia} = 1$ mm was the diaphragm thickness [4]. The measured elastic modulus was $E_{dia} = 3.38 \pm 0.31$ MPa.

3 Post-contact diaphragm physics

To analyze the model's predictions, the dimensionless contact size c/r_{dia} and the dimensionless load $q_{load} r_{dia}^3 / D_{dia}$ were plotted at different lands depths h_{lands}/r_{dia} in Fig. 3. The contact size increased proportionally with the load initially but tapered off gradually. This is due to the diaphragm naturally stiffening as its strain increases.

4 Validation of Pressure-Compensating (PC) Cavity Resistance Model

Computational fluid dynamics (CFD) simulations were performed to validate the PC cavity resistance model.

The simulated fluid volumes' top surface, i.e., the diaphragm, was obtained using Eq. 6 (manuscript). The dimensions were the same as those in prototypes, except for weir depth ($h_{weir} = 0.1$ mm) and weir width ($w_{weir} = 0.3$ mm). Two cavities with

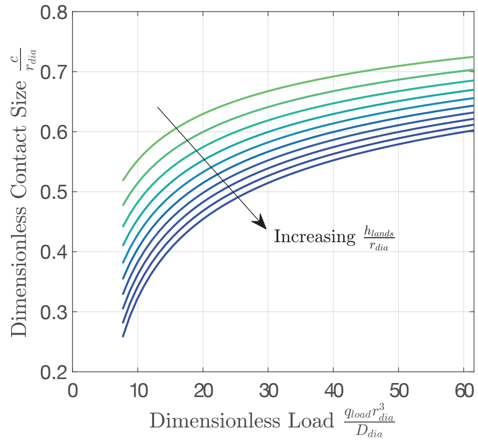

Fig. 3 Dimensionless contact patch size vs. dimensionless load on diaphragm as predicted by post-contact structural submodel. The contact size at each load increases with decreasing lands depth.

lands depth $h_{lands} = 0.6$ and 0.9 mm were modeled, spanning the range of lands depth expected in typical emitter designs. For each lands depth case, three subconfigurations were tested: $w_0/h_{lands} = 0.25, 0.5$, and 0.75 (w_0 is a shorthand notation for $w(r = 0)$). Altogether, the 6 cases spanned the expected design and operating ranges.

The simulations used ANSYS Fluent 2022. The fluid mesh was prepared from polyhedral elements (minimum element length 2.5×10^{-5} m, maximum element length 10^{-4} m). Pressure inlet ($P = 0.1$ bar) and atmospheric outlet ($P_{exit} = 0$) were imposed as boundary conditions. The SST $k-\omega$ model was used to model any turbulence in the flow. The flow rate Q_{CFD} was recorded and used to obtain the reference resistance:

$$K_{dia,CFD} = \frac{P}{Q_{CFD}^2}. \tag{10}$$

The model resistance $K_{dia,Model}$ was obtained from Eq. 14 (manuscript). Unlike the CFD simulations, the modeled geometry was the simplified geometry that is simulated in the 1D model - a cylindrical cavity with a fixed gap δ. Figure 4 plots the comparison of the resistances. Despite the model being 1-dimensional and incorporating simplifications, the agreement was good. On average, the model underpredicts the actual resistance by $10 - 11\%$. Since $K_{dia} < K_{lab}$ over the operating range, this error is considered permissible.

5 Sensitivity Analysis of Weir Resistance

The sensitivity of the total weir resistance K_{weir}, and its components K_{entry} and $K_{internal}$, to weir geometric parameters was inspected. The parameters of interest were h_{weir}, w_{weir}, and L_{weir}. The scaling analysis was performed through a parametric sweep, with one parameter being varied at a time and the remaining being held constant at their maximum value (tabulated in Table 1). In general, the swept range

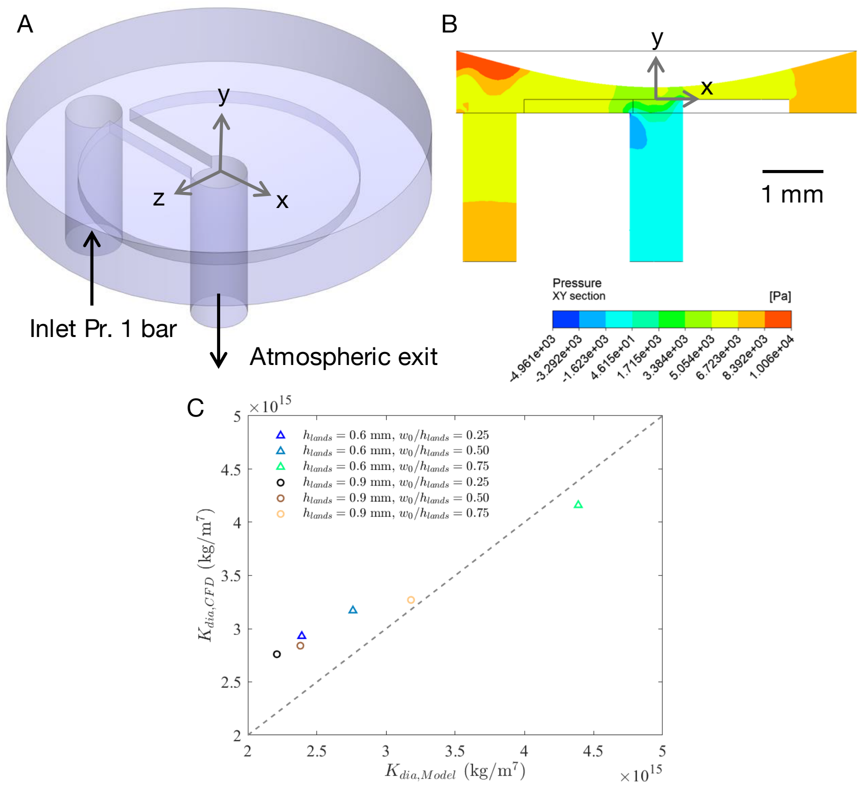

Fig. 4 CFD simulation of PC cavity in pre-contact regime. A) PC cavity fluid volume. B) Pressure contour plot (XY, Z= 0). C) Comparison of CFD predicted vs. analytically modeled diaphragm cavity resistance. The dashed line has a slope of 1, and the closer the plotted points are to it, the better the model-CFD agreement.

was $0.5 - 1\times$ a nominal value. Additionally, the analysis was conducted for three flow rates $Q_{rated} = 1, 1.5$, and 2 L/hr. This was on account of $K_{interal}$ featuring being nonlinear with flow rate Q. All scaling analysis was performed at $P_{in} = 1$ bar.

The results of the scaling analysis are presented in Fig. 5. The following remarks were made:

- Each tested geometry's internal and total weir resistance indeed varied with flow rate. However, this variation was small, indicating that the resistances are weakly nonlinear.
- Resistance is most sensitive to depth and width. It is expected that demand for accuracy in their dimensions will be high.
- The resistance components scale weakly with weir length. The variation in resistance values with pressure must then be driven by the progressive diaphragm shear U.

Table 1 Weir resistance sensitivity analysis. Analysis was performed at $P_{in} = 1$ bar and on a lands cavity having diaphragm stiffness $E_{dia} = 3.38$ MPa, $\nu = 0.49$, lands radius $r_{lands} = 2.5$ mm, and outlet radius $r_{outlet} = 0.5mm$.

Weir Parameter	Nominal Value	Swept Range (× nom. value)
Depth h_{weir}	200 μm	$0.5 - 1$
Width w_{weir}	400 μm	$0.5 - 1$
Length L_{weir}	500 μm	$0.5 - 1$

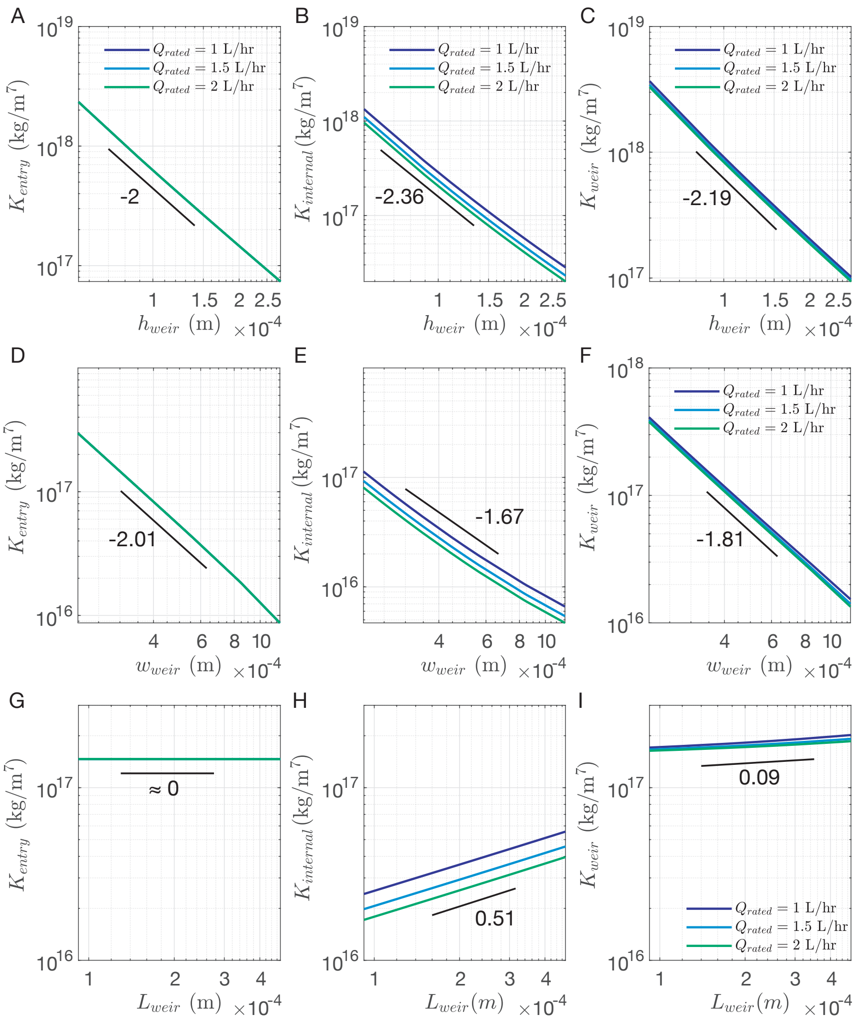

Fig. 5 Results of weir resistance sensitivity analysis.

6 Weir Resistance Model

This is the resistance to flow posed by the weir in the post-contact regime. The weir resistance has two components:

$$K_{weir} = K_{entry} + K_{internal}, \tag{11}$$

where the first term captures the sudden contraction of flow as it enters the weir and the second term arises from wall stresses in the weir. Since the resistance varies with the diaphragm-lands contact and the extent of diaphragm shear into the weir, it is a variable hydraulic resistance.

The entry loss is evaluated using Bernoulli's equation:

$$K_{entry} = \frac{\rho}{2}\left[\frac{1}{A^2} - \frac{1}{A_{outer}^2}\right], \tag{12}$$

where $A = h_{weir} \times w_{weir}$ is the cross-sectional area of the weir (m^2), $A_{outer} = h_{weir} \times \sqrt{r_{lands}^2 - c^2}$ is the chosen representative flow area *outside* the weir in the PC cavity (m^2), and r_{lands} is the lands radius (m). In typical tested geometries, $A \ll A_{outer}$, so K_{entry} reduces to:

$$K_{entry} = \frac{\rho}{2A^2}, \tag{13}$$

The derivation of an expression for internal resistance begins with evaluation of the flow regime (Reynolds number) and whether the flow is developed. In emitter weirs, depth-wise length scale is $h_{weir} \sim 10^{-5}$ m, the width-wise length scale is $w_{weir} \sim 10^{-4}$ m. Based on the work of Duan et al. [5] on flows in ducts with arbitrary cross-sections, the square root of the cross-sectional area was chosen as the transverse length scale L_c rather than the conventional hydraulic diameter. Therefore the L_c and flow speed scale V are:

$$L_c = \sqrt{A} = \sqrt{h_{weir} \times w_{weir}} \sim 10^{-5} \text{ m}, \text{ and } V = \frac{Q}{h_{weir} w_{weir}} \sim 10 - 100 \text{ m/s}, \tag{14}$$

Therefore the Reynolds number is

$$Re = \frac{\rho V L_c}{\mu} \sim 10^3 - 10^4, \tag{15}$$

putting the flow in the regime of transitional to fully turbulent internal flow (critical $Re = 2300$). The development length of the flow is [6]

$$\ell_H = 0.693 L_c Re^{-1/4} \sim 10^{-6} - 10^{-5} \text{ m}. \tag{16}$$

Since the hydrodynamic development length is comparable to the weir length ($0.1 - 0.5 \times 10^{-3}$ m, Fig. 3 in manuscript and also see [7, 8]), the weir flow is classified as a developing turbulent flow.

The derivation procedure of Duan et al. [5] was used here. This starts with a control volume analysis of the weir to obtain the ordinary differential equation to obtain the force balance on an infinitesimal fluid element:

$$\mathrm{d}P_{internal}\, A(x) = \tau_w(x)\mathcal{P}(x)\mathrm{d}x, \tag{17}$$

where $\mathrm{d}P_{internal}$ is the pressure drop over the element length, $\tau_w(x)$ are the wall stresses, $A(x)$ is the local cross-sectional area, and $\mathcal{P}(x)$ is the perimeter of the element. Rearranging the above expression gives an ODE for the pressure drop in the weir:

$$\frac{\mathrm{d}P_{internal}}{\mathrm{d}x} = \tau_w(x)\frac{\mathcal{P}(x)}{A(x)}. \tag{18}$$

The wall stresses can be obtained from empirical friction factors via $\tau_w(x) = f(x)\frac{\rho v^2}{2}$. Substituting this in the above expression,

$$\frac{\mathrm{d}P_{internal}}{\mathrm{d}x} = \frac{\rho v^2}{2}\frac{\mathcal{P}(x)}{A(x)}\frac{fRe}{Re}, \tag{19}$$

$$\implies \frac{\mathrm{d}P_{internal}}{\mathrm{d}x} = \frac{\mu v}{2}\frac{\mathcal{P}(x)}{A(x)}\frac{fRe}{L_c}, \tag{20}$$

$$\implies \frac{\mathrm{d}P_{internal}}{\mathrm{d}x} = \frac{\mu Q}{2}\frac{\mathcal{P}(x)}{A(x)^{5/2}}fRe(x). \tag{21}$$

which is the pressure gradient in a weir with arbitrary, variable cross-section and can be integrated over the streamwise coordinate x. Note that the local streamwise coordinate is $x = 0$ at the weir inlet. fRe is a hydraulic factor that is the product of the Reynolds number and the empirical friction factor. To avoid confusion between fRe and just Re, fRe is replaced by f_H below.

To the best of the Author's knowledge, an expression for f_H in developing turbulent flows is not available. Instead, empirical expressions for f_H in the cases of developing laminar flow (weir entry region) [9] and fully-developed turbulent flow (beyond developed region) [5] were leveraged here:

$$f_H = \begin{cases} \frac{3.44}{\sqrt{x^+}}, & \text{if } x^+ \to 0 \text{ (weir entry)} \\ 0.0767Re^{3/4}, & \text{if } x^+ \to \infty \text{ (weir exit)}, \end{cases} \quad \text{where } x^+ = \frac{x}{\sqrt{A}Re}. \tag{22}$$

x^+ is the scaled streamwise coordinate introduced only for purposes of compactness.

Matching these two asymptotic expressions [9]:

$$f_H = \left[\left(\frac{C_0}{\sqrt{x^+}}\right)^n + C_1^n\right]^{1/n}, \tag{23}$$

where n is the superposition parameter. Here $n = 2$ (for more detail, the reader is referred to [9]). Therefore a continuous expression for fRe is obtained as

$$f_H(x^+) = \left[\left(\frac{3.44}{\sqrt{x^+}}\right)^2 + (0.0767Re^{3/4})^2\right]^{1/2}. \tag{24}$$

Therefore the pressure drop in the weir can be obtained by substituting Eq. 24 into Eq. 21:

$$\frac{\mathrm{d}P_{internal}}{\mathrm{d}x} = \frac{\mu Q}{2}\frac{\mathcal{P}(x)}{A(x)^{5/2}}\left[\left(\frac{3.44}{\sqrt{x^+}}\right)^2 + (0.0767Re^{3/4})^2\right]^{1/2}, \tag{25}$$

$$\implies \Delta P_{internal} = \frac{\mu Q}{2}\int_0^{L_{weir}} \frac{\mathcal{P}(x)}{A(x)^{5/2}}\left[\left(\frac{3.44}{\sqrt{x^+}}\right)^2 + (0.0767Re^{3/4})^2\right]^{1/2} \mathrm{d}x, \tag{26}$$

which is integrated numerically using the trapezoidal method in the model implementation. By definition of hydraulic resistance $K = \Delta P/Q^2$, the internal resistance is then

$$K_{internal} = \frac{\Delta P_{internal}}{Q^2} = \frac{\mu}{2Q}\int_0^{L_{weir}} \frac{\mathcal{P}(x)}{A(x)^{5/2}}\left[\left(\frac{3.44}{\sqrt{x^+}}\right)^2 + (0.0767Re^{3/4})^2\right]^{1/2} \mathrm{d}x. \tag{27}$$

Note that $K_{internal}$ depends on flow rate Q since it features in both the term outside the integral and the integrand through the Reynolds number Re.

7 Incorporation of Diaphragm Shear in Weir Resistance

This is a crucial element of the resistance, particularly at high pressures when the contact radius growth c tapers off due to the natural stiffening of the diaphragm [10, 11]. Diaphragm shear profile $U(x, y, P_{in})$ is 2-dimensional and varies across the span and length of the weir. Evaluation of this profile at every pressure under given flow conditions is a non-trivial problem that is the topic of ongoing research. Instead of deriving a fully resolved U profile, only the characteristic length scale for the shear U_c is used. For a thick compliant wall shearing into a shallow microchannel ($t_{dia}^2 \gg w_{weir}^2$ [12]) this is

$$U_c = \frac{P_{in} w_{weir}(1-\nu^2)}{E_{dia}}. \tag{28}$$

This value is calculated at every pressure in the post-contact regime and is subtracted from the rigid weir depth to obtain a shear-corrected depth

$$h_{corr} = h_{weir} - U_c(P_{in}), \tag{29}$$

Table 2 Dimensions of simulated weir geometries.

Cavity Parameter	Value
Radius r_{dia}	3.72 mm
Transfer Port Radius $r_{transfer}$	0.5 mm
Outlet Radius r_{outlet}	0.5 mm
Lands Radius r_{lands}	2.5 mm
Weir Depth/Weir Width h_{weir}/w_{weir}	0.1/0.3 & 0.2/0.4
Weir Length L_{weir}	$0.1, 0.5$ mm
Lands Depth h_{lands}	$0.6, 0.9$ mm

which is a fixed depth value that is constant over span and length, and varies with pressure. The shear-corrected weir depth is passed into the weir resistance components (Eq. 13 and 27) via the cross-sectional perimeter $\mathcal{P}$ and area A. The perimeter and area are then calculated as:

$$\mathcal{P} = 2(h_{corr} + w_{weir}), \qquad A = h_{corr} \times w_{weir}. \tag{30}$$

This approach simplifies the modeling of the weir at the cost of losing some of the high fidelity that modeling U_{shear} will grant. However, as evidenced from the discussion in the manuscript Sec. 3, despite this simplification the model can continue to predict the overall performance of the emitter with just $8-14\%$ RMSE.

8 Simulation Check of Weir Model

The entire PC cavity was modeled to capture both K_{entry} and $K_{internal}$. Table 2 summarizes the simulated geometries. Since weir cross-section affects resistance most strongly, two weir cross-sections spanning the expected design range were tested: $h_{weir}/w_{weir} = (0.1\text{ mm}/0.3\text{ mm})$ and $(0.2\text{ mm}/0.4\text{ mm})$. Each cross-section was tested at two weir lengths: $L_{weir} = 0.1$ mm and 0.5 mm. This covered most of the expected weir length range. Finally, these weirs were tested in two PC cavities having lands depth $h_{lands} = 0.6$ and 0.9 mm, bringing the total number of tested cases to 8.

Simulations were performed using ANSYS FLUENT 2022. The meshes were composed of polyhedral elements (minimum element length 2.5×10^{-5} m, maximum element length 10^{-4} m). Selective mesh refinement was performed in the weir region, where the minimum element size was 2.5×10^{-6} m. Since boundary layer effects were expected to be important in the weir flow, boundary layer meshing was performed as well, with 5 imposed layers at the default growth rate of 1.2. Pressure inlet ($P = 1$ bar) and atmospheric outlet ($P_{exit} = 0$) were imposed as boundary conditions. The SST $k-\omega$ model was used to model turbulence in the flow. The flow rate Q_{CFD} was recorded and used to obtain the simulated resistance:

$$K_{weir,CFD} = \frac{P}{Q_{CFD}^2}. \tag{31}$$

To calculate the analytical resistance, Q_{CFD} was plugged into Eq. 20 (manuscript) to calculate $K_{internal}$. The entry resistance is independent of the flow rate. Figure

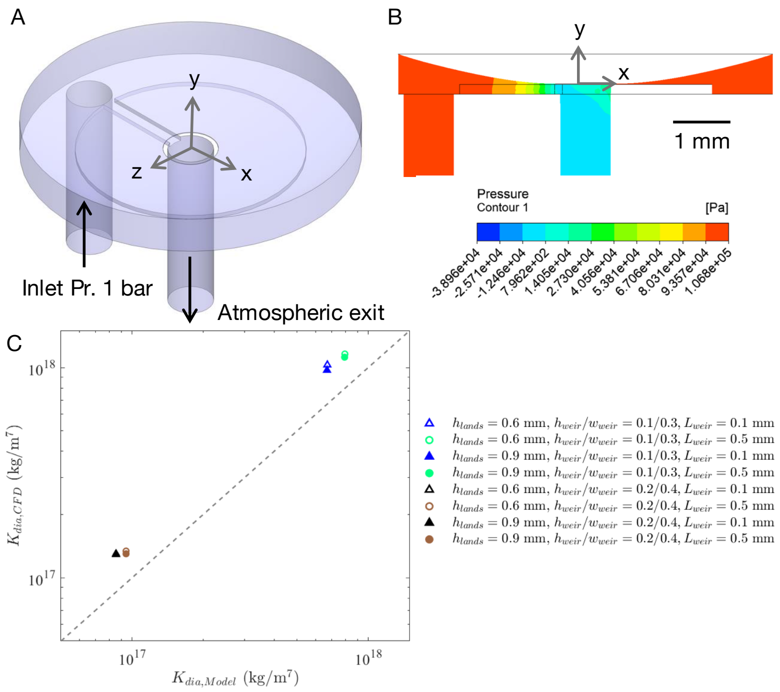

Fig. 6 CFD simulations of post-contact PC cavity. A) Simulated geometry. B) Pressure contour plot (XY, Z= 0) demonstrating that pressure distribution under diaphragm is largely uniform outside the weir (pictured case: $h_{lands} = 0.6$ mm, $h_{weir} = 0.1$ mm, $w_{weir} = 0.3$ mm, $L_{weir} = 0.1$ mm). Most of the pressure drop is localized in the weir entry region. C) Comparison of CFD predicted vs. analytically modeled diaphragm weir resistance. The dashed line has a slope 1, and the closer the plotted points are to it, the better the model-CFD agreement.

6 plots the simulated resistance vs. analytical resistance. The following observations were made:

- Analytical resistance and simulated resistance showed agreement, but this agreement decreases as the weir becomes progressively more resistive.
- As expected, changing the weir cross-section had the largest impact on resistance.
- The weir length has a small effect on resistance aligned with scaling results.
- The lands depth had a negligible effect on the weir resistance value.

9 Evaluation of Labyrinth Design and Resistance

The geometry required to support the desired resistance was determined using an empirical labyrinth design theory derived in Ghodgaonkar et al. [13]. This theory identified three geometric parameters for tuning K_{lab} - the tip gap b_{tip} (m), depth h_{lab} (m), and number of tooth units N_{teeth}. The three key parameters were set to meet

Table 3 Critical dimensions, desired resistance, and measured resistance of labyrinths in LPE prototypes. All labyrinths had $N_{teeth} = 11$ pairs of tooth units.

Desired Flow Rate (L/hr)	b_{tip} (μm)	h_{lab} (mm)	Desired K_{lab} (kg/m^7)	Measured K_{lab} (kg/m^7)
1	75	0.76	2.621×10^{17}	2.071×10^{17}
1.5	0	0.75	3.666×10^{17}	3.202×10^{17}
2	125	1	1.052×10^{17}	1.057×10^{17}

the target K_{lab} in the expression:

$$\hat{K}(\hat{b}, \hat{h}, N_{teeth}) = \frac{0.327\, N_{teeth}}{\hat{h}^{1.842}} \left(-0.064\hat{b}^2 - 0.166\hat{b} + 0.6\right), \tag{32}$$

where $\hat{K} = K_{lab} \times 10^{-17}$, $\hat{b} = b_{tip} \times 10^4$, and $\hat{h} = h_{lab} \times 10^3$. The chosen values for the three flow rate variants are listed in Table 3. The remaining parameters form the nominal geometry of the labyrinth and were set by manufacturing, clogging, etc. considerations. To adopt the design theory directly, the labyrinths prepared had the same nominal geometry as those in [13], and also had the same tooth count $N_{teeth} = 11$.

Measurement of K_{lab}: To isolate the resistance of the labyrinth from the remaining emitter features, a bottom block with an enlarged outlet that overlapped with the transfer channel was used. This allowed water to exit straight out of the transfer channel rather than re-enter the PC cavity. Flow rate was recorded using the test procedure detailed in Manuscript Sec. 3.

Figure 7 plots the flow rate and resistance data for each labyrinth. Resistance was obtained by calculating the ratio P_{in}/Q^2 at every setpoint, and the mean of these measured values was used in the model. When a power law curve was fit to each of the flow rate-pressure data, the power varied between $0.5 - 0.51$, showing excellent agreement with the expected value of 0.5.

10 Stability Analysis of FSI Algorithm

A perturbation test was performed to check the stability of the model. For this the Newton calculation step in the FSI algorithm was adjusted to

$$Q_{i,j} = Q_{i,j-1} + \underbrace{\epsilon Q_{i,j-1}}_{\text{perturbation}} - \phi \frac{f(Q_{i,j-1})}{f'(Q_{i,j-1})}, \tag{33}$$

where $\epsilon \ll 1$ is a small perturbation factor. Note that ϵ was a constant, but the total perturbation $\epsilon Q_{i,j}$ was a variable, since the flow rate changes at every Newton step. The convergence of the Newton calculations at various pressures was inspected at different perturbation factors. It was expected that the shape of the convergence curve $Q_{i,j}$ vs. j and the converged flow rate would not vary significantly between perturbed and unperturbed states in a stable scheme.

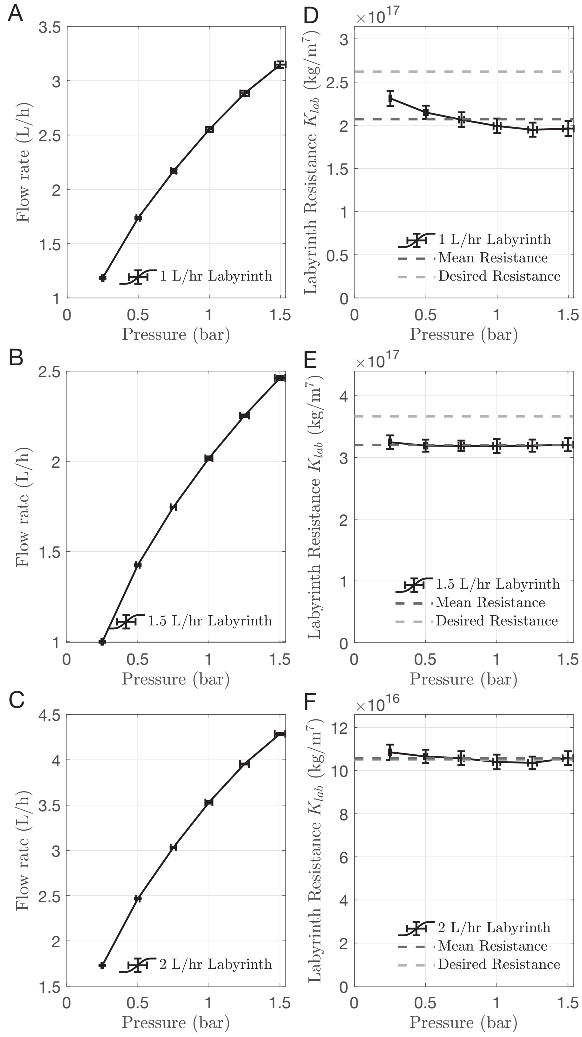

Fig. 7 Experimental characterization of prototype labyrinths. A,B,C) Flow rate-pressure data was collected for all three labyrinths, and processed to yield (D,E,F) resistance-pressure data. The mean resistance fell within 26% of the desired value for all cases. The mean measured resistance was used to generate model predictions. The vertical error bars are the standard deviation in measurements over 4 repeats, and the horizontal error bars are ±10% of the pressure setpoint (observed variability).

The test was performed at three pressures: $P_i = 0.35, 0.50$, and 0.75 bar. These pressures were selected to cover contact-initiation, near-post-contact ($c \ll r_{lands}$), and post-contact ($c < r_{lands}$) operation of the emitter respectively. The 2 L/hr prototype developed for the model validation was used as a representative design in the case study.

Test 1: Varying the perturbation factor (ϵ). This test was performed with a pressure step size $P_{i+1} - P_i = 0.05$ bar, a radial grid count of $N_r = 200$ (the number

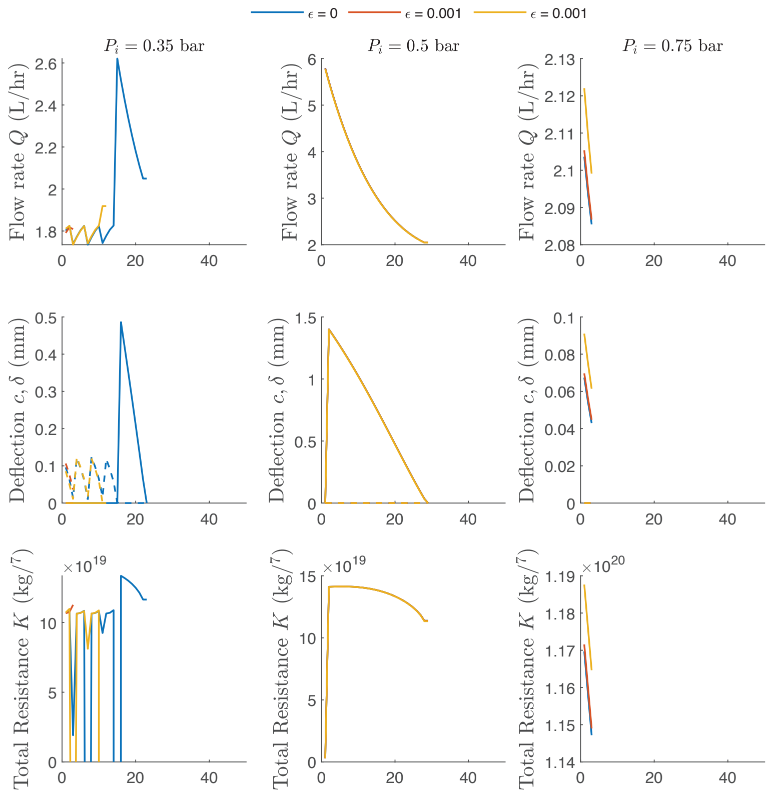

Fig. 8 Perturbation test of 2 L/h emitter simulation at at $P_i = 0.35, 0.5$, and 0.75 bar, with $N_r = 200, P_{i+1} - P_i = 0.05$ bar. The Y-axis plots the Newton step number j. In the deflection panels, the dashed lines represent the diaphragm-lands gap δ and the bold lines represent the contact radius c. At 0.5 bar, the convergence contours overlap completely indicating that the perturbation does not affect the scheme. At 0.75 bar, the convergence contours shift only after a large perturbation is imposed.

of discrete points at which deflection was calculated), and three perturbation factors $\epsilon = 0$ (unperturbed reference), 10^{-3}, and 10^{-2}. Figure 8 shows how the flow rate, contact patch size c, and total resistance K_{tot} converged. The following observations were made:

- At $P_i = 0.75$ bar, $Q_{i,j}$ vs. j did not vary much with ϵ. Since the contact radius is non-zero this indicates that the *post*-contact implementation of the model is stable.
- At $P_i = 0.5$ bar, once again $Q_{i,j}$ vs. j did not vary much with ϵ. Interestingly it was observed that at the start of calculations, the model enters the post-contact regime $c > 0$, but gradually converges to a pre-contact state $c = 0$. This indicated that contact initiation and activation did not occur at the same pressure.
- At $P_i = 0.35$ bar, the converged solution varied a lot with ϵ, indicating instability.

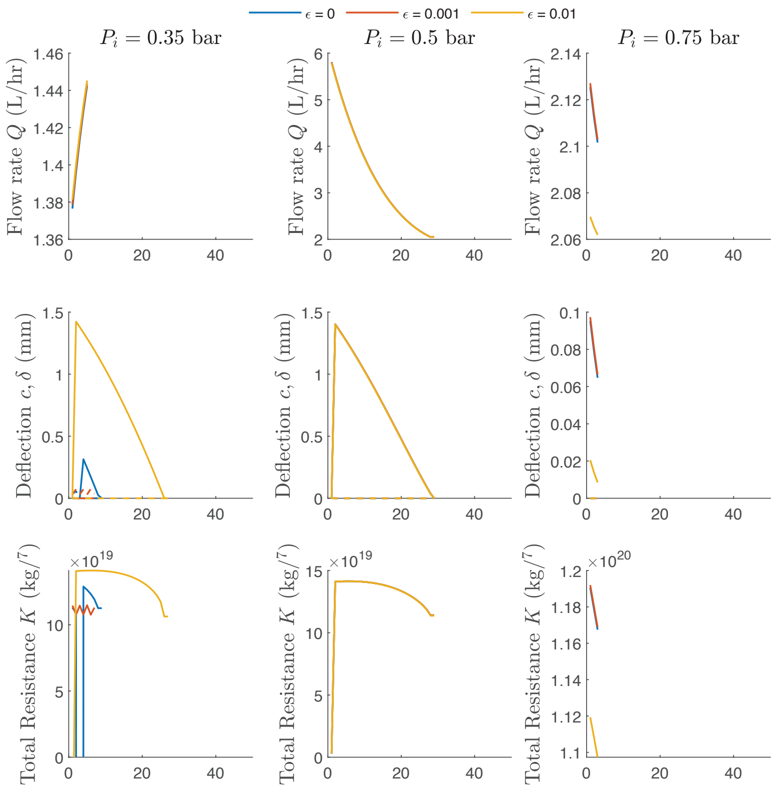

Fig. 9 Perturbation test of 2 L/h emitter simulation at $P_i = 0.35, 0.5$, and 0.75 bar, this time with $N_r = 400, P_{i+1} - P_i = 0.025$ bar. The Y-axis plots the Newton step number j. In the middle panels, the dashed lines plot the diaphragm-lands gap δ and the bold lines plot the contact radius c.

At $P_i = 0.35$ bar the diaphragm is at the threshold of $w(r_{outlet}) \approx h_{lands}$, i.e., it is almost in contact with the outlet edge. Beyond this point, the model is unable to smoothly transition between to post-contact states and so has difficulty converging to a stable solution. This is attributed to how the deflection states are calculated in the code: 1) pre-contact deflection shape is calculated, 2) deflection at the radial node closest to the outlet radius is found, and 3) then the code checks if the deflection at this point is greater than the lands depth. If it is, the model re-calculates deflection as a contacted diaphragm. To check if this issue could be avoided by improving the spatial resolution N_r and pressure step resolution $P_{i+1} - P_i$, another test was performed.

Test 2: Varying the grid size and pressure step. The above test was re-run with $N_r = 400$ and $P_{i+1} - P_i = 0.025$ bar (Fig. 9). However, the general observations from test 1 did not change. Based on these observations, it was concluded the model is unstable in the near-contact regime.

Despite this numerical instability in the model, it continues to predict the overall emitter performance to within $8 - 14\%$ error. This is because the instability exists only in a narrow band of pressures near the contact initiation stage.

11 Farmer Interviews in the Jordan Valley for Case Study

Seven semi-structured interviews were conducted with farmers in the Jordan River valley to learn their current drip irrigation practices, challenges they experience, and evaluate whether/how low-pressure emitters (LPEs) would assist them. The interview structure was intentionally semi-structured to create opportunities for farmers to share insights and challenges unprompted. Jordan River valley was selected as a location for interviews due to it being a beachhead market for LE-DI – high solar irradiance makes this region ripe for the adoption of solar-powered irrigation; terrain variations create irrigation non-uniformity that could be alleviated through the use of PC drip irrigation; and high electricity costs and small pump sizes limit the adoption of conventional PC drip irrigation. Additionally, storyboards depicting the potential benefits of LE-DI were prepared and presented to farmers during the interviews. Figure 10 presents the storyboards in English, but they were translated into Arabic by local interview partners.

11.1 The Questionnaire

At the start of every interview, the farmers signed a consent form, and the date and location of the interview were recorded. Not all questions were asked of all farmers. The questionnaire was adjusted based on farmer responses. List of questions included:

1. Do you use drip irrigation on the entire farm? If not, why not? (crop, soil, energy?)
2. What kinds of emitters do you use now, and have you used different ones in the past? (online/inline OR PC/NPC)
3. If yes, what made you switch between emitters?
4. What emitter brand do you use, and how did you pick this? (e.g., do other community members also use it?)
5. How do you decide when to buy a new dripline? (What does dripline failure look like?)
6. How long do your drip lines typically last? When you see dripline failure, what kind of issues do you see? (e.g., clogging, physical damage?)
7. What size is your pump? (physical size and/or power)
8. How is the pump powered? (solar/fuel/grid)
9. What pressure is your pump set to, and how do you decide what it should be?
10. (The storyboards were typically presented at this stage before continuing.) If you were deciding whether to purchase this (LPEs) or not, what questions would you have or what information would you want?
11. How do you think you would benefit from low-pressure drip irrigation?
12. Would you reinvest the saved power expenses into the farm somehow?

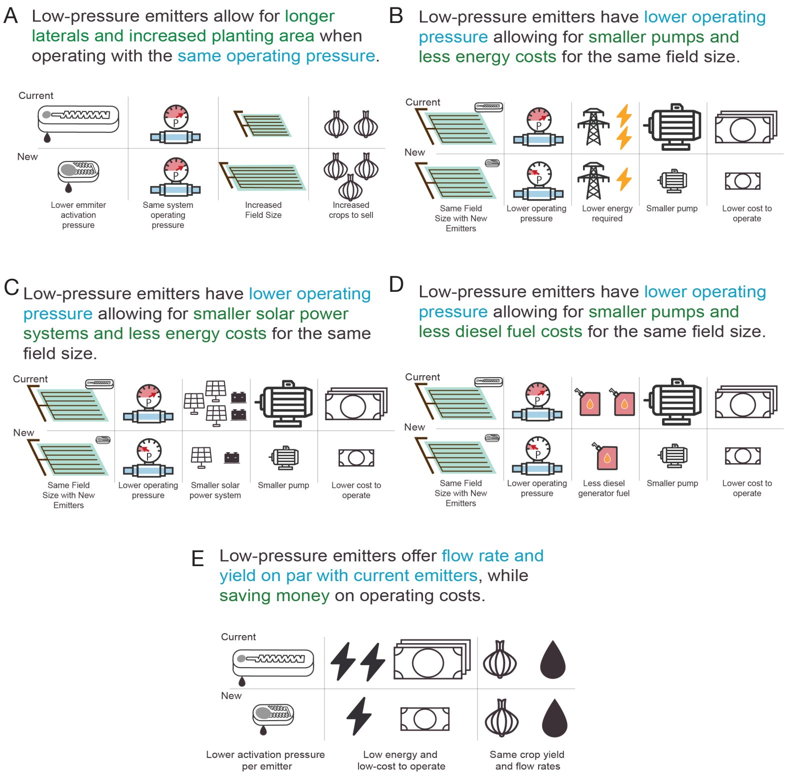

Fig. 10 Emitter storyboards presented to farmers in Jordan River valley. Storyboard A presents one potential benefit of using LP-PC drip irrigation, longer laterals at no added pumping cost. Storyboards B-D present the most direct benefit of LP-PC drip irrigation, the power savings achieved from reducing activation pressure. The alternatives are grid, solar, or diesel-powered systems. The final storyboard E presented the reduced operating cost while reassuring farmers that there would be no loss in harvest or water delivered to crops.

13. Would you choose to shift to solar panels or expand solar panel usage on your farm if your new emitters needed less power/pressure?
14. Would you consider investing in low-pressure drip emitters if you had to replace your current pump?
15. If you used low-pressure emitters, would you want to run multiple sections at the same time with a larger pump or shift to smaller pumps to run each section as you usually do?
16. How did you choose your power source (diesel/grid/solar), and would you prefer to switch sources if it took less power to operate your emitters?
17. Do you have any other questions or thoughts?

11.2 Interview Results

1. All 7 stored water drawn from a surface water source in an open pond. Water was then pumped to the field.
    - Five out of seven farmers used canal water fed by a dam;
    - One of the 5 canal water users supplemented this water with desalinated well water
    - Another one of the 5 canal water users supplemented this with natural spring water.
    - Remaining 2/7 used spring water only.
2. At least 2 farmers had to pump water from their storage pond to their furthest section, being 200 m away.
3. While some farmers used multiple pumps to irrigate, the range was $7.5 - 20$ HP, with most pumps being 15 HP (5), or 10 HP (4).
4. Six out of seven farmers used non-pressure compensating (NPC) emitters, with at least 4/6 using 4 L/h (at 1 bar) emitters and at least 2/6 using 8 L/h. 1/6 used both 4 and 8 L/h emitters.
5. One farmer used only 2 L/h PC emitters that were pressurized to $1.5 - 2$ bar to achieve uniformity.
6. At least one farmer's emitters were spaced by 0.4 m, although $0.3 - 0.4$ m is a common spacing in the region according to local irrigation experts.
7. Farmers grew vegetables (peppers, tomatoes, potatoes) or citrus crops.
8. At least one farmer had a maximum lateral length of 30 m, and at least 6/7 farmers used drip lines with 16 mm inner diameter.

Challenges faced by farmers:

1. At least 4/7 farmers (all using NPC) faced challenges due to irrigation non-uniformity arising from the hilly terrain.
2. Hilly terrain (2/4) or insufficient pump head constrained the farmer's ability to irrigate larger or multiple sections simultaneously.
3. One farmer compensated for this by varying tube sizes across the field.
4. At least one farmer was discouraged from using solar panels due to the high cost of installation.
5. At least 2 farmers complained of poor plastic material durability.

Farmer preferences:

1. Six farmers (all using NPC emitters) would prefer to extend their laterals into uncultivated land or consolidate field sections if they had access to low-pressure PC emitters.
2. One farmer was already planning to invest in PV panels; they noted the benefit of low-pressure emitters reducing panel cost as attractive.
3. One farmer explicitly mentioned their preference to use low-pressure emitters to expand their farm rather than switch to solar panels.

References

[1] Hou, G., Wang, J., Layton, A.: Numerical methods for fluid-structure interaction—a review. Communications in Computational Physics **12**(2), 337–377 (2012)

[2] The Toro Company: Toro Blueline PC Technical Documentation. (2022). The Toro Company. https://cdn.thetorocompany.com/api/assetstorage/623_d43351d4-b20e-413a-b2d5-b7feb22c5f49

[3] Young, W.C., Budynas, R.G., Sadegh, A.M., *et al.*: Roark's Formulas for Stress and Strain vol. 7. McGraw-hill New York, ??? (2002)

[4] Ghodgaonkar, A. Private communication with The Toro Company (2020–2022)

[5] Duan, Z., Yovanovich, M.M., Muzychka, Y.S.: Pressure Drop for Fully Developed Turbulent Flow in Circular and Noncircular Ducts. Journal of Fluids Engineering **134**(6), 061201 (2012) https://doi.org/10.1115/1.4006861 https://asmedigitalcollection.asme.org/fluidsengineering/article-pdf/134/6/061201/5719588/061201_1.pdf

[6] Kundu, P.K., Cohen, I.M., Dowling, D.R., Capecelatro, J.: Fluid Mechanics. Elsevier, ??? (2024)

[7] Sokol, J., Narain, J., Costello, J., McLaurin, T., Kumar, D., Winter, A.G.: Analytical model for predicting activation pressure and flow rate of pressure-compensating inline drip emitters and its use in low-pressure emitter design. Irrigation Science **40**(2), 217–237 (2022) https://doi.org/10.1007/s00271-022-00771-5

[8] Shamshery, P., Winter, A.G.: Shape and form optimization of on-line pressure-compensating drip emitters to achieve lower activation pressure. Journal of Mechanical Design **140**(3) (2018) https://doi.org/10.1115/1.4038211

[9] Muzychka, Y.S., Yovanovich, M.M.: Pressure Drop in Laminar Developing Flow in Noncircular Ducts: A Scaling and Modeling Approach. Journal of Fluids Engineering **131**(11), 111105 (2009) https://doi.org/10.1115/1.4000377 https://asmedigitalcollection.asme.org/fluidsengineering/article-pdf/131/11/111105/5579641/111105_1.pdf

[10] Chen, X., Wei, Z., Ma, C., Wei, C.: Flow characteristics and diaphragm deformation of pressure-compensating drip irrigation emitters. Irrigation and Drainage **70**(5), 996–1009 (2021) https://doi.org/10.1002/ird.2601

[11] Narain, J., Winter V, A.G.: A hybrid computational and analytical model of inline drip emitters. Journal of mechanical design **141**(7) (2019) https://doi.org/10.1115/1.4042613

[12] Wang, X., Christov, I.C.: Theory of the flow-induced deformation of shallow compliant microchannels with thick walls. Proceedings of the Royal Society A **475**(2231), 20190513 (2019) https://doi.org/10.1098/rspa.2019.0513

[13] Ghodgaonkar, A., Welsh, E., Judge, B., Winter V, A.G.: An empirical design theory for compact drip irrigation emitters. Irrigation Science, 1–21 (2025) https://doi.org/10.1007/s00271-024-00987-7